An Anode-Free Sodium All-Solid-State Battery

Grayson Deysher[1], Jin An Sam Oh[2], Yu-Ting Chen[1], Baharak Sayahpour[1], So-Yeon Ham[1], Diyi Cheng[1], Phillip Ridley[2], Ashley Cronk[1], Sharon Wan-Hsuan Lin[2], Kun Qian[2], Long Hoang Bao Nguyen[2], Jihyun Jang[2,3,*], Ying Shirley Meng[2,4,*]

[1] Program of Materials Science and Engineering, University of California San Diego; La Jolla, CA 92093, United States.

[2] Department of NanoEngineering, University of California San Diego; La Jolla, CA 92093, United States.

[3] Department of Chemistry, Sogang University; Seoul, 04107, Republic of Korea.

[4] Pritzker School of Molecular Engineering, The University of Chicago; Chicago, IL 60637, United States.

* Corresponding authors: jihyunjang@sogang.ac.kr, shirleymeng@uchicago.edu

Abstract

Anode-free batteries possess the optimal cell architecture due to their reduced weight, volume, and cost. However, their implementation has been limited by unstable anode morphological changes and anode-liquid electrolyte interface reactions. An electrochemically stable solid electrolyte can solve these issues by enabling the deposition of dense sodium metal. Furthermore, a novel type of aluminum current collector can achieve intimate solid-solid contact with the solid electrolyte which allows highly reversible sodium plating and stripping at both high areal capacities and current densities, previously unobtainable with conventional aluminum foil. A sodium anode-free all-solid-state battery full-cell is demonstrated with stable cycling for several hundred cycles. This cell architecture serves as a future direction for other battery chemistries to enable low-cost, high-energy-density, and fast charging batteries.

Introduction

Recent years have shown an increasing demand for electric vehicles as well as energy storage devices for large-scale grid applications. Batteries are critical for enabling these technologies and although they have improved significantly since the introduction of the first commercial lithium-ion battery in 1990 [1], further enhancements are needed to enable higher energy density and lower cost energy storage systems. While lithium batteries may be optimized further to address these two challenges, there remains an intrinsic limitation. Lithium is geographically concentrated and has experienced a significant increase in price as the demand for batteries grows [2]. Sodium-based materials, on the other hand, are significantly less expensive and more widely available. While

sodium batteries are often assumed to sacrifice energy density in favor of lower cost, in this work we show that lower-cost sodium batteries may still achieve a high energy density comparable to current lithium systems due to the natural advantages of several sodium materials compared to their lithium counterparts.

To compete with the high energy density possessed by lithium-ion batteries, large specific capacity and high cell voltage are needed while using sodium chemistry. To maximize cell voltage the anode with the lowest reduction potential should be used – sodium metal. However, sodium metal is extremely soft and highly reactive making it impractical to produce foils on a large scale. A recently popularized idea is the use of an anode-free cell architecture [3]. Unlike conventional batteries, anode-free batteries are those in which no anode active material is used. Rather than using carbon- or alloy-based anode materials to store sodium ions during cell charging, anode-free batteries rely on the electrochemical deposition of sodium metal directly onto the surface of a current collector (Fig. 1a). This not only retains the low reduction potential of sodium metal, thus enabling higher cell voltage, but also lowers the cell cost and increases energy density due to the removal of the anode active material (Fig. 1b).

However, many challenges have prevented the use of such a cell architecture. The deposition of sodium metal in conventional organic liquid electrolyte batteries is known to produce a porous or mossy-like morphology [4]. Additionally, liquid electrolytes commonly react with the deposited sodium forming a solid-electrolyte interphase (SEI) [5,6]. Continuous sodium morphological changes during cycling inevitably result in the continuous formation of SEI which steadily consumes the sodium inventory [7]. Although several strategies have been explored including modifications to the liquid electrolyte [8], they have yielded only moderate improvements with many demonstrating only tens of cycles and/or low initial Coulombic efficiencies (ICE). Instead, a better approach is to utilize solid-state electrolytes. Due to their solid nature, the solid electrolyte separator layer is limited to a planar two-dimensional contact area with the negative electrode current collector (Fig. 1a). This can facilitate less solid-electrolyte interfacial reactions and can enable the deposition of dense sodium metal.

To enable an anode-free sodium solid-state battery, four conditions must be met (Fig. 1c). First, an electrochemically stable or highly passivating electrolyte is needed to avoid the consumption of active sodium inventory due to the formation of a SEI layer. Second, intimate and robust solid-solid interface contact between the solid electrolyte and the current collector is needed for repeated sodium plating/stripping. Any void between the materials will prevent electron transfer and Na^0 deposition cannot occur. Third, a dense solid-state electrolyte separator is needed. It is known that pores, cracks, and imperfections can promote the growth of metal filaments through the separator resulting in cell short-circuiting [9–13]. Fourth, the current collector needs to be highly dense. While porous current collectors have been shown to be effective in liquid electrolyte cells due to their higher surface area and lowered local current densities [14,15], these current collectors cannot be used in solid-state cells. Unlike liquid electrolytes, solid-state electrolytes cannot flow into the pores of the current collector, therefore sodium plated inside the pores will become trapped due to the lack of sodium conduction pathways during stripping.

In this work, we seek to meet these four requirements to enable an anode-free sodium all-solid-state battery. An electrochemically stable sodium borohydride solid electrolyte was found to achieve near-perfect contact with a pelletized aluminum current collector. Morphological evaluation found that the borohydride electrolyte can achieve a nearly fully dense structure by cold pressing which inhibited the penetration of sodium dendrites and enabled cycling at current densities exceeding 6 mA•cm^{-2}. Additionally, the aluminum current collector was also found to be highly dense thus meeting the four requirements outlined above. As a proof-of-concept, an anode-free sodium all-solid-state battery with $NaCrO_2$ as the cathode was cycled for 400 cycles with an average Coulombic efficiency of 99.96%. This work strives to be framework for the future development of sodium and other battery chemistries with high energy densities and offers a description of the critical factors governing their electrochemical performance.

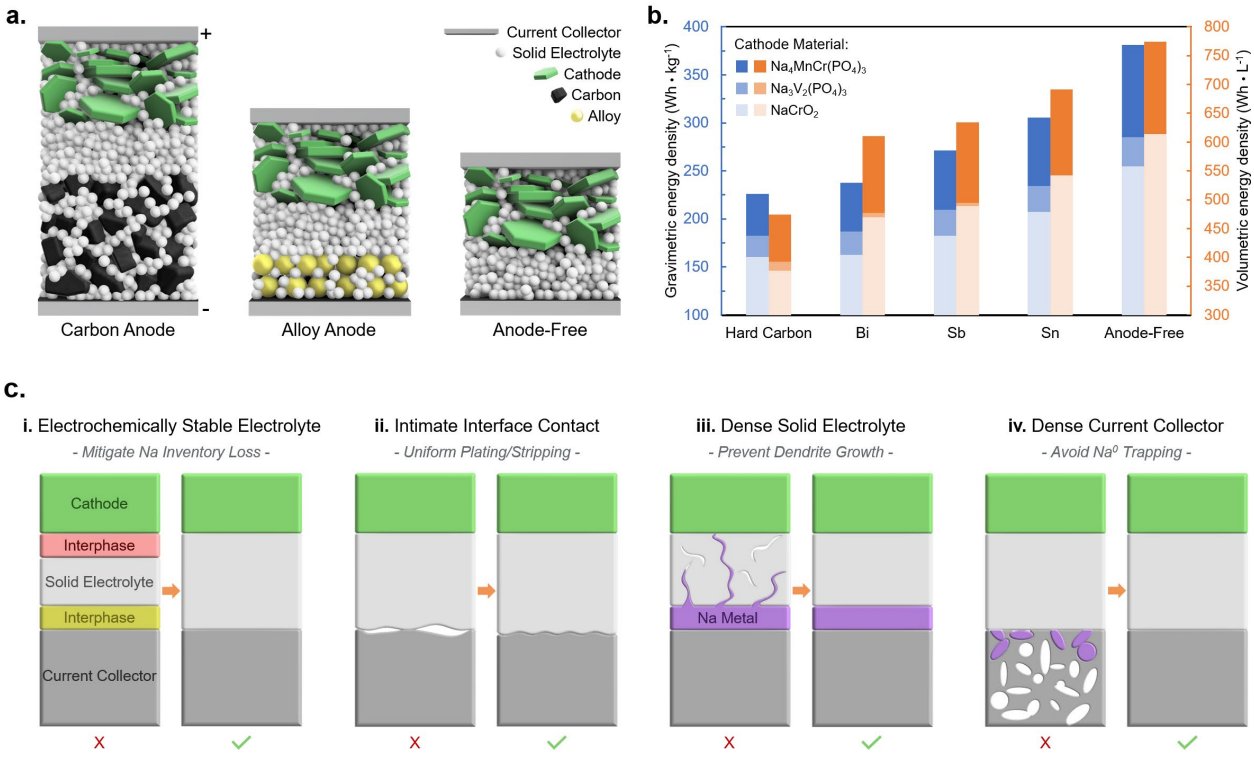

Fig. 1. Anode-free schematics and energy density calculations. a) Cell schematic for carbon anodes, alloy anodes, and an anode-free configuration. b) Theoretical energy density comparison for various sodium anode materials. Values used for the calculations can be found in *table S1*. c) Schematic illustrating the requirements for enabling an anode-free all-solid-state battery.

Results and Discussion

Electrochemically Stable Electrolyte

An anode-free half-cell was assembled with the commonly used Na_3PS_4 (NPS) solid electrolyte paired with an aluminum foil current collector and Na_9Sn_4 counter electrode (fig. S1). The ICE was 4%. This can be attributed to the reduction of NPS at low potential forming Na_3P [16], which is a known mixed conductor, leading to continuous SEI growth and the irreversible consumption of sodium inventory. To solve the electrochemical instability, a sodium borohydride solid electrolyte ($Na_4B_{10}H_{10}B_{12}H_{12}$ (NBH)) was used as the separator. NBH has previously been shown to be electrochemically stable against sodium metal [16,17]. Sodium was again electrochemically plated onto the aluminum foil and then stripped away, resulting in a higher ICE of 64% (Fig. 2a). This demonstrates the importance of using an electrochemically stable solid electrolyte in anode-free cells. However, the efficiency when using NBH remained unacceptably low, therefore other aspects of the anode-free architecture require improvement.

Intimate Interface Contact

Metal foils are by far the most common current collectors used in batteries, however only a small area of the foil was plated with sodium (Fig. 2a), which was confirmed to be metallic sodium by XRD (fig. S2). This indicates that there is not sufficient solid-solid contact between the solid electrolyte and the aluminum foil current collector as sodium can only deposit where there is a connection between the incoming Na^+ from the solid-state electrolyte and the electron from the current collector. After stripping, sodium was still observed on the foil, thus explaining the relatively low ICE (Fig. 2a). This can be attributed to poor interface contact between the solid electrolyte, sodium metal, and foil current collector which resulted in incomplete stripping of the sodium. This indicates that conventional aluminum foil does not meet the intimate interface contact requirement, resulting in poor reversibility.

To improve the solid-solid interfacial contact between the solid electrolyte and current collector, pelletized aluminum was pressed onto the solid electrolyte separator during cell fabrication in the same process as when using aluminum foil (Fig. 2b). Aluminum powder can easily conform to the variable topography of the solid electrolyte separator layer which is formed during the cell fabrication process (Fig. 2c). This current collector will be referred to as aluminum pellet. When cycled under the same conditions, the half-cell ICE was significantly improved to 93%. When cells were disassembled after plating and after one full cycle, the uniformity of the sodium metal distribution on the current collector surface was found to be greatly improved. Even after plating 1 $mAh{\cdot}cm^{-2}$, which theoretically amounts to an 8.5 μm Na metal layer, the deposition was already uniformly distributed. This implies that the aluminum powder can form a more uniform and intimate contact with the solid electrolyte separator across the entire cell area compared to traditional aluminum foil. This was further demonstrated with electrochemical impedance spectroscopy which showed a lower interfacial resistance when using the aluminum pellet current collector (Fig. 2d). Furthermore, the aluminum pellet was shown to evenly distribute the applied stack pressure across the entire area of the cell which was found by inserting pressure-

sensitive paper in between the current collector and solid electrolyte layers during cell fabrication (Fig. 2e). This likely also helps in uniformly spreading the soft sodium metal as it is plated in cells under stack pressures (10 MPa stack pressure used for this study) well above the yield strength of sodium (~0.2 MPa) [18].

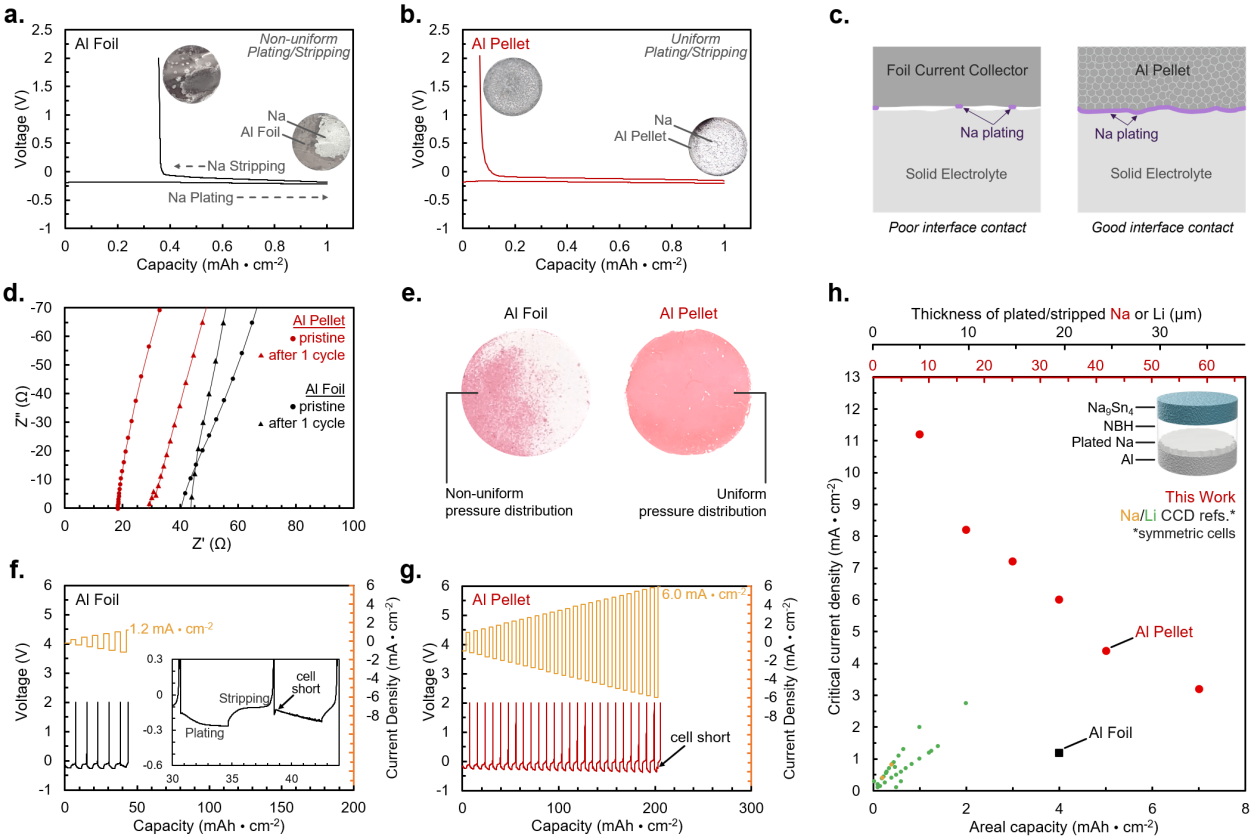

Fig. 2. **Al pellet comparison with Al foil**. Plating/stripping behavior at 1 mA•cm^{-2} current density for a) Al foil and b) Al Pellet current collectors. c) Schematic illustrating the ability of aluminum powder to form intimate contact with the solid electrolyte layer. d) Impedance measurements before and after cycling Al foil and Al pellet cells. e) Pressure paper showing the distribution of pressure over the cell area when using Al foil and Al pellet current collectors. Critical current density when cycling 4 mAh•cm^{-2} capacity with f) Al foil and g) Al pellet current collectors. h) Critical current density evaluation as a function of areal capacity at room temperature when using an Al pellet current collector. Cycling data can be found in fig. S4. Literature data that utilized cold-pressed solid electrolytes is added for comparison [19–41].

Due to the improved contact and sodium plating uniformity, the applied current will be distributed over a larger area compared to when using aluminum foil. As high current density promotes the formation of dendrites [42–44], which can lead to cell short-circuiting, lowering the local current density enables cell cycling at higher total currents. When using aluminum foil and cycling with 4 mAh•cm^{-2} capacity between the electrodes, the critical current density was found to be 1.2 mA•cm^{-2} (Fig. 2f). The cell failed during the sodium plating step, and the Na_9Sn_4 counter electrode

was found to cycle at much higher currents (fig. S3) therefore this critical current density can be attributed to failure by sodium dendrite penetration through the electrolyte during plating. When using the aluminum pellet current collector, the critical current density increased to 6.0 mA•cm^{-2} (Fig. 2g). Interestingly, compared to previously reported critical current density values for cold pressed cells (Fig. 2h) our data shows successful cycling at significantly higher currents, even when using an aluminum foil current collector. Most previously reported critical current density values are ≤ 2 mA•cm^{-2} at ≤ 2 mAh•cm^{-2} capacity. This indicates that there may be another factor governing the high current ability of these cells, besides the type of current collector.

Dense Solid Electrolyte

Anode-free cells rely on the nature of the interface between the current collector and the solid electrolyte. Therefore, the solid electrolyte properties are also important to consider when assessing this type of cell architecture. Focused-ion beam milling scanning electron microscopy (FIB-SEM) was used to evaluate the morphology of the NBH solid electrolyte after cold pressing to form the separator layer (Fig. 3a-c). The NBH electrolyte separator exhibited an extremely dense morphology. The crosshatch line pattern textured on the surface is due to the imperfect titanium plunger used to press the solid electrolyte layer (fig. S5). More importantly, only a few rounded micron-sized surface pores were observed indicating good compaction without the need for high temperature sintering (Fig. 3b). The cross-section of the NBH was intentionally milled at the spot of one of the surface pores to examine how deep they protrude into the electrolyte layer. It was found that the pores have a rounded morphology that does not extend further than ~1 μm (Fig. 3c). In addition to the intimate interface contact achieved by using the aluminum pellet current collector, the dense morphology of NBH also contributes to the observed high critical current densities. It is known that imperfections in the solid electrolyte separator such as pores and cracks can result in dendrite penetration and cell short circuiting [9–13]. Without these imperfections, it becomes much more difficult for sodium to penetrate the solid electrolyte layer (Fig. 3d). To compare with lithium solid electrolytes, $Li_4B_{10}H_{10}B_{12}H_{12}$ (LBH) was selected as a direct comparison with NBH as it has also been shown to achieve an electrochemically stable interface with lithium metal [45]. Li_6PS_5Cl (LPSCl) was also selected due to its common use in lithium solid-state batteries. These solid electrolytes were found to exhibit porous morphologies after cold pressing (fig. S6). When these electrolytes were used as the separator in lithium half-cells, the cells short circuited shortly after the plating step began and could only be successfully cycled at much lower current densities (0.1 mA•cm^{-2}). This can be attributed to the soft lithium creeping into the surface cracks of the separators [12], which can result in current concentrations at the tips of the lithium metal filaments and further exacerbate the filament growth through the solid electrolyte [46]. NBH materials on the other hand have been shown to be softer than their lithium counterparts [47], but previously there have been no visual observations of the highly dense morphology that can be achieved by cold pressing when using NBH. The high sodium critical current density can be attributed to this newly revealed ability of this borohydride electrolyte.

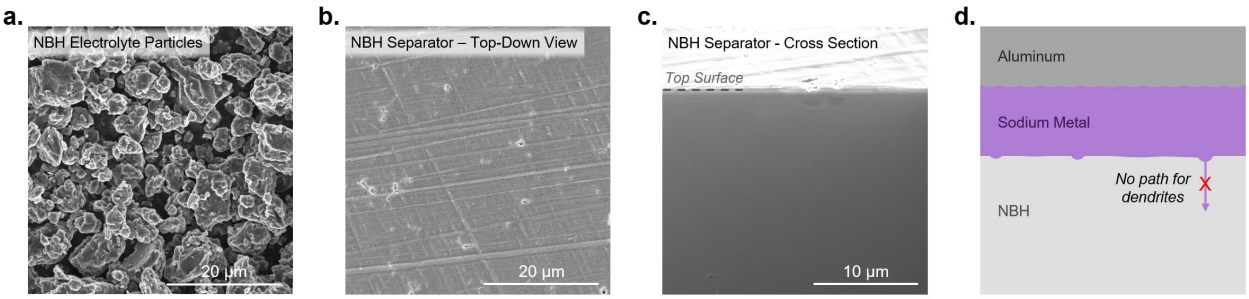

Fig. 3. **Evaluation of NBH morphology**. SEM of a) NBH particles and b) top view of the NBH separator after cold pressing. c) FIB-SEM cross section view of NBH separator. d) Schematic illustrating the propensity of sodium to deposit without forming dendrites through the electrolyte.

Dense Current Collector

To probe the effect of the current collector morphology, aluminum, copper, and titanium were selected for comparison due to their common use in solid-state battery research as current collectors and cell materials. Like aluminum, copper and titanium do not form alloys with sodium, ensuring that they will only act as a current collector. Using a half-cell configuration, the plate/strip ICEs were significantly different (Fig. 4a-c). There were also small slope regions observed in the voltage curves during the initial stages of plating when using copper and titanium. This is attributed to the surface oxide layers present on these metals that react with the incoming sodium forming an oxide (fig. S7). This likely contributes partially to the irreversible capacity due to the high bonding energy between sodium and oxygen although the thin nature of the surface oxides and the small capacity observed within the slope regions indicates that it is not the major factor affecting the overall irreversibility. After repeated cycling the aluminum cells exhibited the highest capacity retention followed by copper, and then titanium which had the lowest capacity retention (Fig. 4d). As the solid electrolyte-current collector interface is known to play a critical role in the cyclability of solid-state anode-free cells (Fig. 2), the surface topography of the three current collectors was compared using optical profilometry (Fig. 4e-g). While all three current collectors exhibited slightly different surface textures, likely correlated to their powder morphology (fig. S8), the roughness of their surfaces were close in value; 0.98 µm, 1.05 µm, and 0.90 µm for aluminum, copper, and titanium respectively. Therefore, their degree of contact with the solid electrolyte separator should be similar. This indicates that the reversibility differences may be due to a bulk current collector effect rather than an interface variation.

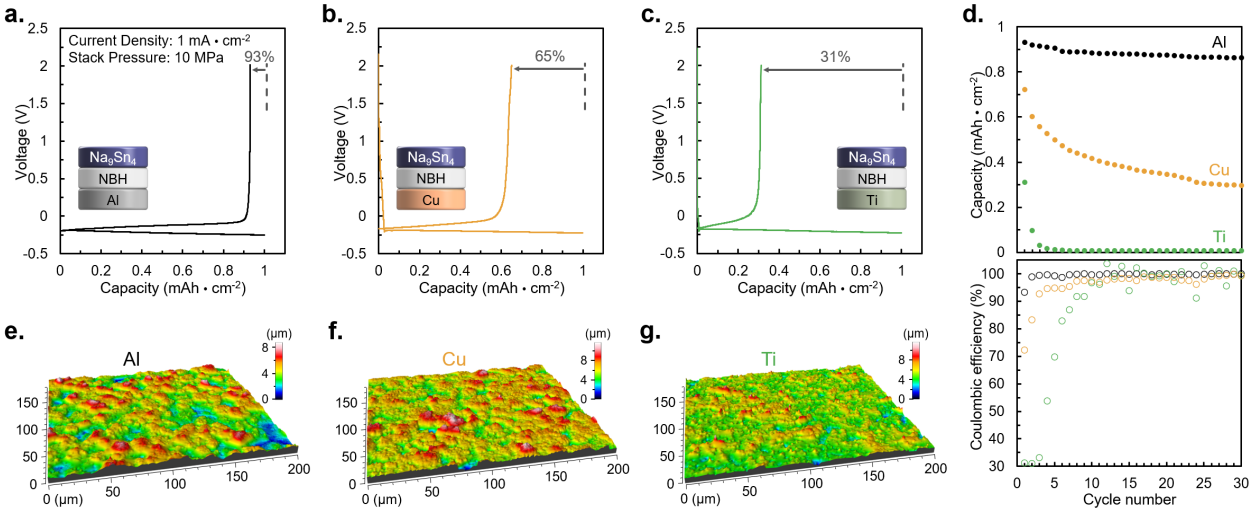

Fig. 4. **Evaluation of various pelletized current collectors**. First cycle plating/stripping voltage curves of half-cells using a) Al, b) Cu, and c) Ti pellet current collectors. d) Electrochemical performance of the same three cells over 30 cycles. Optical profilometry measurements of the surface topography of e) Al, f) Cu, and g) Ti pellet current collectors.

To evaluate the bulk morphology of the three current collectors, FIB-SEM was used to image their cross-sections. As shown in Fig. 5a-c, the aluminum current collector was almost fully dense. By using the weight and volume of the pellet, the porosity of the aluminum was calculated to be 0 – 3%. In contrast, the copper current collector contained many micron-sized pores (19 – 23% porosity), and similarly, the titanium current collector contained many larger pores (34 – 35% porosity). To establish a quantitative trend comparison between these three materials, several current collectors were fabricated at various pressures and their porosities were determined (Fig. 5d). It was found that aluminum powder can densify more easily than copper and titanium powders which can be explained by the varying mechanical properties of these three materials in which aluminum possesses the lowest Vickers hardness (~160 MPa) compared to copper (~370 MPa) and titanium (~970 MPa) [48]. To evaluate the potential impact of the current collector porosity on the reversibility of sodium plating/stripping, FIB-SEM was used again on cycled cells after one plate/strip cycle. These results (Fig. 5e-g) show that when pores are present in the current collector, sodium metal can become trapped inside during plating. Since there is no liquid electrolyte present and the solid electrolyte separator is unable to flow into the current collector pores, the sodium in the pores becomes ionically insulated after the sodium metal at the solid electrolyte-current collector interface is stripped away (Fig. 5h). This results in a sodium trapping effect which can be seen in the sodium energy dispersive X-ray spectroscopy (EDS) maps (Fig. 5e-g). Therefore, the use of aluminum was found to be critical to enable reversible plating/stripping, as it is soft enough to become highly dense after cold pressing during cell fabrication.

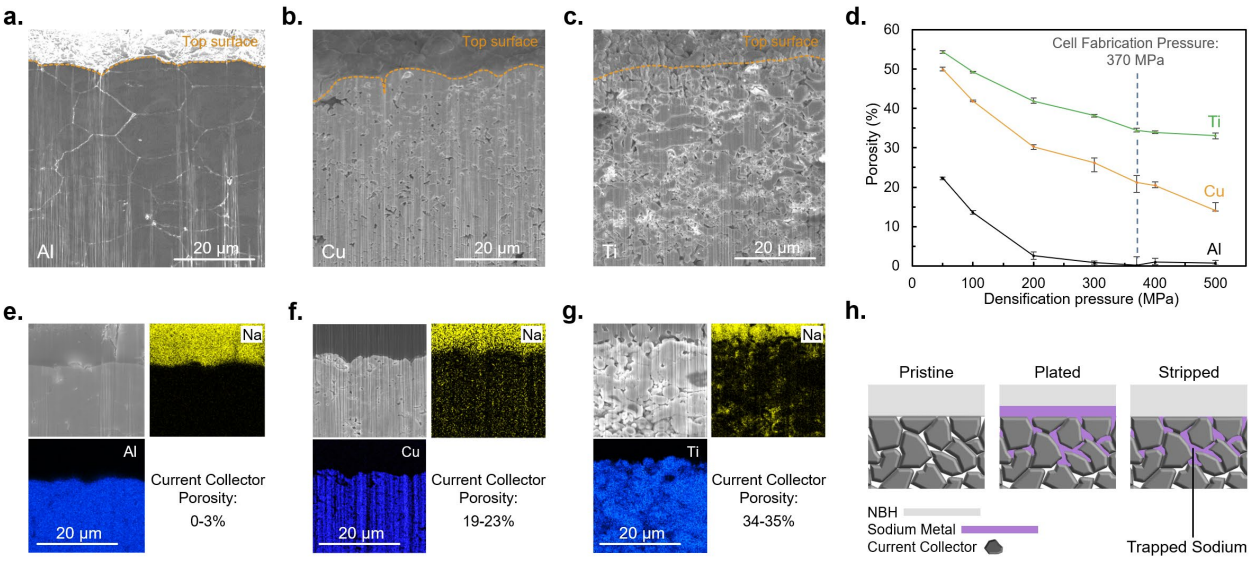

Fig. 5. **Evaluation of pelletized current collector morphologies**. FIB-SEM cross section views of pristine a) Al, b) Cu, and c) Ti pellet current collectors. d) Current collector porosity as a function of fabrication pressure. FIB-SEM cross section views of e) Al, f) Cu, and g) Ti current collectors after one plate/strip cycle with EDS mapping. h) Schematic of Na trapping mechanism for porous current collectors.

Stack Pressure and Sodium Morphology

Beyond enabling reversible cycling in an anode-free architecture, there are other important practical cell performance considerations to evaluate. Often, high stack pressures (50 – 250 MPa) are used for solid-state cell cycling [12,49–53]. This is not a commercially viable option because larger area cells, such as 3×3 cm^2, can require forces exceeding 10 tonnes (Fig. 6c). It is likely that no battery pack casing will be able to achieve such high pressures safely and consistently without using a heavy construction and thus lowering the cell energy density. Instead, lower pressure cycling should become the norm for solid-state battery research. Due to their low moduli, bulk alkali metal anodes are known to work well at lower pressures [54,55]. To assess the effect of cell stack pressure on cyclability in this anode-free cell configuration, half-cells were cycled at 5, 10, 15, and 20 MPa of constant stack pressure (Fig. 6a-b). When 10 – 20 MPa was used, the cells exhibited very similar reversibility and capacity retention. This indicates that pressures higher than 10 MPa are not needed. 5 MPa cycling was found to be less reversible. As no noticeable difference in the cyclability of Na_9Sn_4 was observed at 5 and 10 MPa (fig. S3), the change in anode-free half-cell performance at 5 MPa can be attributed to the anode-free side. The lower reversibility of anode-free cycling at 5 MPa can be attributed to the difficulty in maintaining intimate solid-solid contact between the current collector, sodium metal, and solid electrolyte which is essential for complete stripping of the deposited sodium. However, lower pressures such as 5 and 1 MPa can still be enabled using a slightly elevated cycling temperature (fig. S9). At 40 °C, the efficiency of 5 and 1 MPa cells became similar to that of 10 MPa presumably due to the softening of metallic sodium, similar to that observed with lithium [56], which can facilitate the retention of intimate solid-solid interfaces even at lower pressures.

Areal capacity is also important to consider as higher areal capacities result in higher overall energy densities by maximizing the active: inactive material ratio. Using 10 MPa stack pressure, it was found that cycling 1, 3, and 7 mAh•cm^{-2} capacity of sodium, corresponding to 8.8, 26.5, and 61.9 μm of deposited sodium respectively, exhibited very similar reversibility and capacity retention (Fig. 6d-e). Furthermore, similar plating/stripping efficiencies were observed for both 10- and 13-mm diameter cells, which indicates that larger cell areas are also possible (fig. S10). The sodium morphology was evaluated using cryogenic FIB-SEM (Fig. 6f). The sodium was found to form a dense and intimate interface with both the NBH and the Al which is critical for enabling sufficient ion and electron transfer respectively. To evaluate the bulk sodium morphology after plating, a cell was examined using cryo-FIB-SEM after plating 7 mAh•cm^{-2} capacity (Fig. 6g). The electrochemically deposited sodium metal contained no pores in the area examined. This dense morphology is unique to this solid-state cell architecture under stack pressure compared to the mossy sodium observed when using liquid electrolytes at very low pressures. To evaluate the sodium morphology over a larger scale, an X-ray computed tomography scan was performed on a smaller 4 mm diameter cell after plating 7 mAh•cm^{-2} capacity (Fig. 6h). The sodium was found to be uniformly distributed across the surface of the current collector (Fig. 6i) and no significant morphological features were observed. This can be attributed to the homogenous plating of sodium due to the intimate and electrochemically stable interface which is responsible for enabling the highly efficient plating/stripping observed for areal capacities as high as 7 mAh•cm^{-2}.

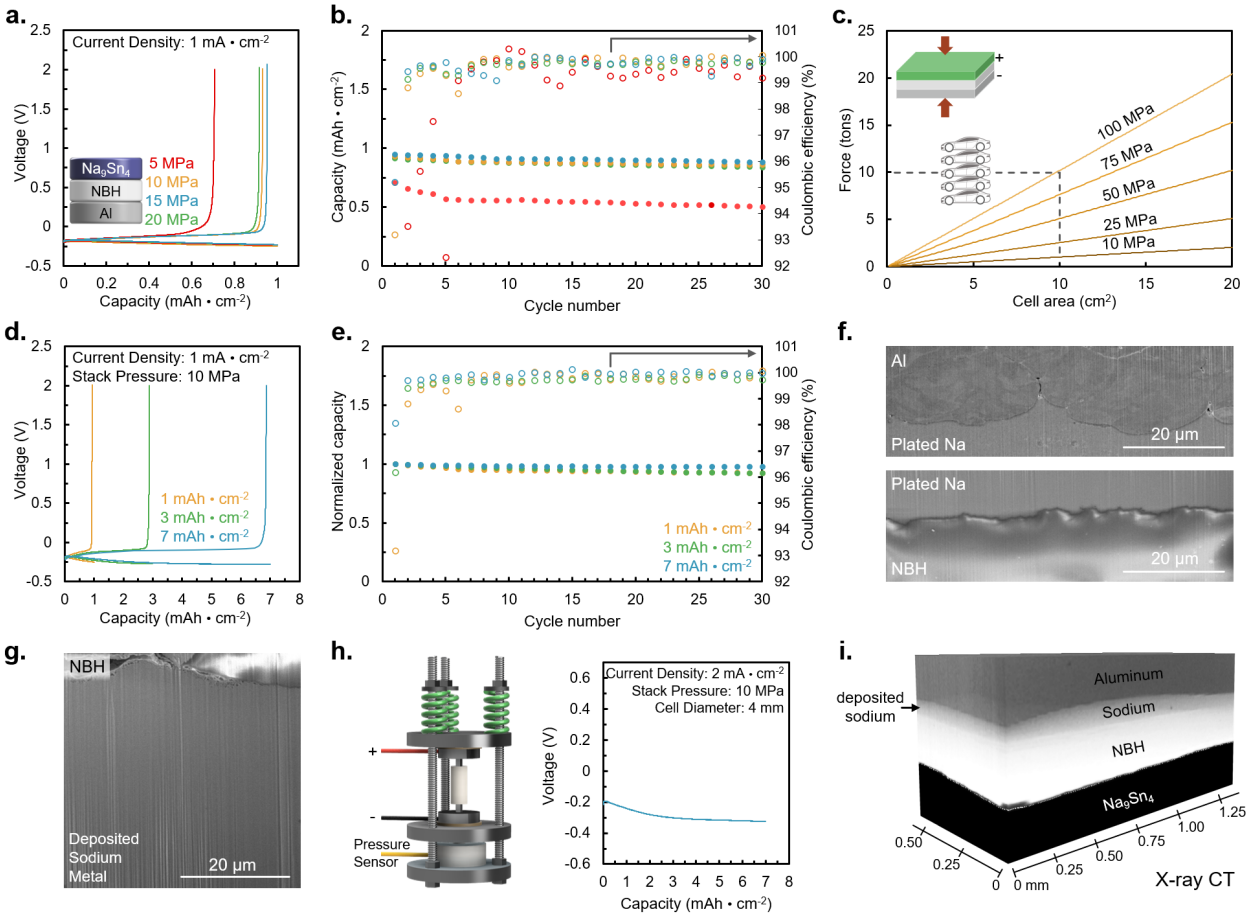

Fig. 6. **Effects of cell stack pressure and areal capacity**. a) Voltage profiles for Na_9Sn_4 | NBH | Al half-cells cycled at 5, 10, 15, and 20 MPa. b) Capacity retention during extended cycling of the same cells. c) Force required to achieve various stack pressures. d) Voltage profiles for Na_9Sn_4 | NBH | Al half-cells cycled with 1, 3, and 7 mAh•cm^{-2} capacities. e) Capacity retention during extended cycling of the same cells. Cryo-FIB/SEM images of the f) Na-Al and Na-NBH interfaces and g) thick plated sodium. h) Cell holder schematic and cycling data for a custom 4 mm diameter X-ray computed tomography cell. i) X-ray computed tomography scan of 7 mAh•cm^{-2} plated sodium metal.

Anode-Free Sodium All-Solid-State Full-Cell

To demonstrate an anode-free sodium all-solid-state full-cell, a low cost $NaCrO_2$ cathode was used and paired with a $Na_{0.625}Y_{0.25}Zr_{0.75}Cl_{4.375}$ catholyte that is known to be electrochemically stable against $NaCrO_2$ [57]. When cycled at room temperature, the cell experienced noticeable polarization (Fig. 7a). To overcome the slow cathode kinetics, the full-cell was cycled at a higher temperature of 40 °C (Fig. 7b). This improved the cathode capacity utilization at higher currents (Fig. 7c). Additionally, a constant voltage hold can be added at the charged state to maximize the extraction of capacity from the cathode. With this protocol, the ICE of 93% was achieved which is similar to the ICE achieved in anode-free half cells (Fig. 7d). The cell maintained stable cycling for 400

cycles with a capacity retention of 70% (Fig. 7e) which is due to the high average Coulombic efficiency of 99.96%. This performance is attributed to the combination of the aluminum pellet current collector with the sodium borohydride solid electrolyte. This demonstrates the significant improvement when using an aluminum pellet compared to conventional aluminum foil which can only cycle for tens of cycles before losing most of its capacity (Fig. 7f). While higher cathode loadings and thinner solid electrolyte layers will be needed to enable the full potential of this cell architecture, this truly anode-free cell design demonstrates the effectiveness of dense solid electrolyte and current collector morphologies as well as a robust interface between them.

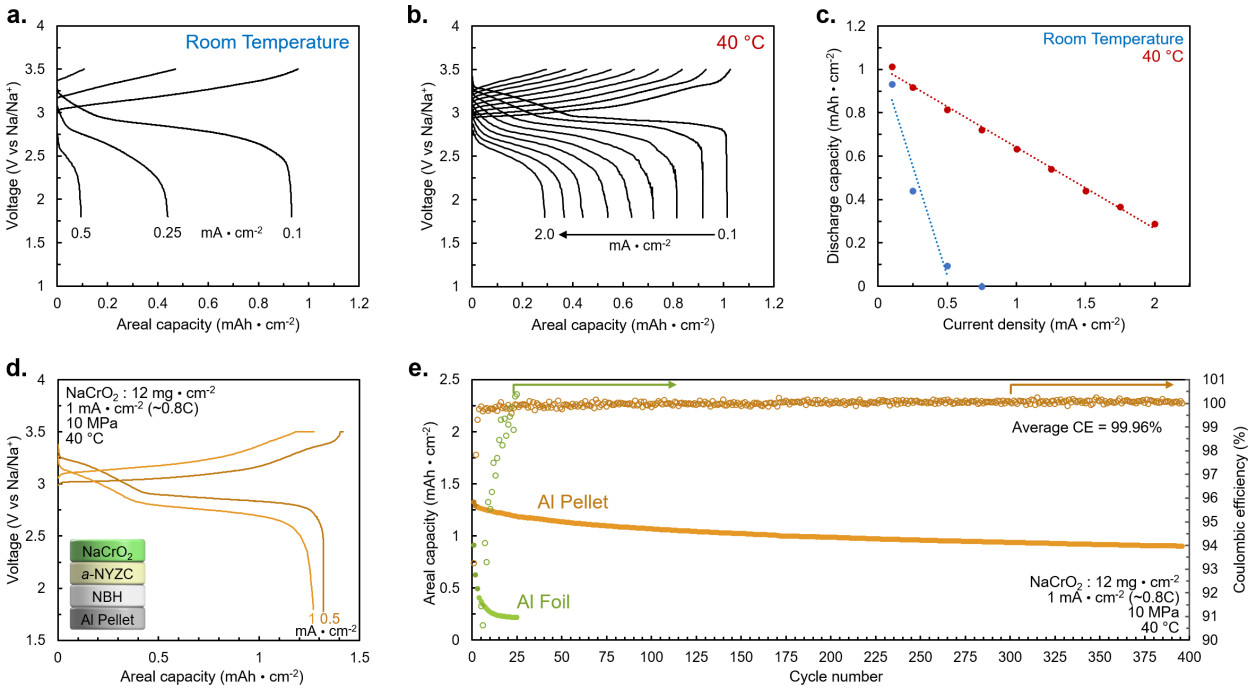

Fig 7. **Anode-free sodium all-solid-state full-cell cycling**. Voltage curves of a sodium anode-free half-cell cycled at various currents at a) room temperature and b) 40 °C. Voltage curves for the first three formation cycles are not shown. c) Cathode capacity as a function of current density. d) Voltage curves of a sodium anode-free solid-state full-cell including a constant voltage hold at 3.5 V and e) cell capacity over 400 cycles for the same cell combined with Al foil data for comparison. $NaCrO_2$ cathode was used in all cells.

Conclusion

In this work we enable stable cycling in an anode-free all-solid-state battery architecture which can potentially lead to a significant increase in energy density. A pelletized aluminum current collector was shown to enable improved solid-solid interface contact with the borohydride-based solid electrolyte. This intimate interface enabled significantly higher current density cycling. By pairing the dense aluminum pellet current collector with a sodium borohydride solid electrolyte, reversible cycling was achieved for capacities as high as 7 mAh•cm^{-2} (62 µm of sodium) due to

the electrochemically stable and dense solid electrolyte. Using a low-cost $NaCrO_2$ cathode, an anode-free sodium all-solid-state full-cell battery was demonstrated to cycle several hundred cycles. This work elucidates the four critical factors that govern the electrochemical performance of anode-free solid-state cell designs to guide future developments of high energy all-solid-state batteries. We believe that this work can guide the discovery and implementation of other anode-free battery chemistries and serve as an example that sodium can compete with and complement traditional lithium-ion batteries.

Acknowledgements

This work was performed in part at the San Diego Nanotechnology Infrastructure (SDNI) of UCSD, a member of the National Nanotechnology Coordinated Infrastructure, which is supported by the National Science Foundation (grant ECCS-2025752). The authors acknowledge the use of facilities and instrumentation at the UC Irvine Materials Research Institute (IMRI), which is supported in part by the National Science Foundation through the UC Irvine Materials Research Science and Engineering Center (DMR-2011967). Specifically, the XPS work was performed using instrumentation funded in part by the National Science Foundation Major Research Instrumentation Program under grant no. CHE-1338173. Xe plasma FIB experiments were conducted at the University of Southern California in the Core Center of Excellence in Nano Imaging. We also acknowledge the use of the UCSD Crystallography Facility.

Funding: Funding to support this work was provided by the National Science Foundation through the Partnerships for Innovation (PFI) grant no. 2044465.

Competing Interests: A patent application for this work has been filed by G.D. and Y.S.M. through UC San Diego's Office of Innovation and Commercialization.

References

1. Nishi, Y. The Dawn of Lithium-Ion Batteries. *Electrochem. Soc. Interface* **25**, 71 (2016).
2. Hirsh, H. S. *et al.* Sodium-Ion Batteries Paving the Way for Grid Energy Storage. *Advanced Energy Materials* **10**, 2001274 (2020).
3. Qian, J. *et al.* Anode-Free Rechargeable Lithium Metal Batteries. *Advanced Functional Materials* **26**, 7094–7102 (2016).
4. Tang, S. *et al.* A room-temperature sodium metal anode enabled by a sodiophilic layer. *Nano Energy* **48**, 101–106 (2018).
5. Matios, E., Wang, H., Wang, C. & Li, W. Enabling Safe Sodium Metal Batteries by Solid Electrolyte Interphase Engineering: A Review. *Ind. Eng. Chem. Res.* **58**, 9758–9780 (2019).
6. Gao, L., Chen, J., Chen, Q. & Kong, X. The chemical evolution of solid electrolyte interface in sodium metal batteries. *Science Advances* **8**, eabm4606 (2022).
7. Wang, Y. *et al.* Developments and Perspectives on Emerging High-Energy-Density Sodium-Metal Batteries. *Chem* **5**, 2547–2570 (2019).
8. Lu, Z., Yang, H., Yang, Q.-H., He, P. & Zhou, H. Building a Beyond Concentrated Electrolyte for High-Voltage Anode-Free Rechargeable Sodium Batteries. *Angewandte Chemie International Edition* **61**, e202200410 (2022).
9. From Lithium-Metal toward Anode-Free Solid-State Batteries: Current Developments, Issues, and Challenges - Heubner - 2021 - Advanced Functional Materials - Wiley Online Library. https://onlinelibrary.wiley.com/doi/full/10.1002/adfm.202106608.
10. Shen, F., Dixit, M. B., Xiao, X. & Hatzell, K. B. Effect of Pore Connectivity on Li Dendrite Propagation within LLZO Electrolytes Observed with Synchrotron X-ray Tomography. *ACS Energy Lett.* **3**, 1056–1061 (2018).

11. Kazyak, E. *et al.* Li Penetration in Ceramic Solid Electrolytes: Operando Microscopy Analysis of Morphology, Propagation, and Reversibility. *Matter* **2**, 1025–1048 (2020).
12. Luo, S. *et al.* Growth of lithium-indium dendrites in all-solid-state lithium-based batteries with sulfide electrolytes. *Nat Commun* **12**, 6968 (2021).
13. Yuan, C. *et al.* Coupled crack propagation and dendrite growth in solid electrolyte of all-solid-state battery. *Nano Energy* **86**, 106057 (2021).
14. Liu, S. *et al.* Porous Al Current Collector for Dendrite-Free Na Metal Anodes. *Nano Lett.* **17**, 5862–5868 (2017).
15. Yun, Q. *et al.* Chemical Dealloying Derived 3D Porous Current Collector for Li Metal Anodes. *Advanced Materials* **28**, 6932–6939 (2016).
16. Deysher, G. *et al.* Evaluating Electrolyte–Anode Interface Stability in Sodium All-Solid-State Batteries. *ACS Appl. Mater. Interfaces* **14**, 47706–47715 (2022).
17. Duchêne, L. *et al.* A highly stable sodium solid-state electrolyte based on a dodeca/deca-borate equimolar mixture. *Chemical Communications* **53**, 4195–4198 (2017).
18. Wang, M. J., Chang, J.-Y., Wolfenstine, J. B. & Sakamoto, J. Analysis of elastic, plastic, and creep properties of sodium metal and implications for solid-state batteries. *Materialia* **12**, 100792 (2020).
19. Schlenker, R. *et al.* Understanding the Lifetime of Battery Cells Based on Solid-State Li6PS5Cl Electrolyte Paired with Lithium Metal Electrode. *ACS Appl. Mater. Interfaces* **12**, 20012–20025 (2020).
20. Yang, Z. *et al.* Developing a high-voltage electrolyte based on conjuncto-hydroborates for solid-state sodium batteries. *J. Mater. Chem. A* **10**, 7186–7194 (2022).
21. Jin, M., Yang, Z., Cheng, S. & Guo, Y. Fast Sodium-Ion Conduction in a Novel Conjuncto-Hydroborate of Na4B20H18. *ACS Appl. Energy Mater.* **5**, 15578–15585 (2022).

22. Kasemchainan, J. *et al.* Critical stripping current leads to dendrite formation on plating in lithium anode solid electrolyte cells. *Nat. Mater.* **18**, 1105–1111 (2019).
23. Su, Y. *et al.* A more stable lithium anode by mechanical constriction for solid state batteries. *Energy Environ. Sci.* **13**, 908–916 (2020).
24. Bonnick, P. *et al.* A high performance all solid state lithium sulfur battery with lithium thiophosphate solid electrolyte. *J. Mater. Chem. A* **7**, 24173–24179 (2019).
25. Fan, X. *et al.* Fluorinated solid electrolyte interphase enables highly reversible solid-state Li metal battery. *Science Advances* **4**, eaau9245 (2018).
26. Liang, J. *et al.* An Air-Stable and Dendrite-Free Li Anode for Highly Stable All-Solid-State Sulfide-Based Li Batteries. *Advanced Energy Materials* **9**, 1902125 (2019).
27. Zhang, Z. *et al.* All-in-one improvement toward Li6PS5Br-Based solid electrolytes triggered by compositional tune. *Journal of Power Sources* **410–411**, 162–170 (2019).
28. Garcia-Mendez, R., Mizuno, F., Zhang, R., Arthur, T. S. & Sakamoto, J. Effect of Processing Conditions of 75Li2S-25P2S5 Solid Electrolyte on its DC Electrochemical Behavior. *Electrochimica Acta* **237**, 144–151 (2017).
29. Zhang, Z. *et al.* One-step solution process toward formation of Li6PS5Cl argyrodite solid electrolyte for all-solid-state lithium-ion batteries. *Journal of Alloys and Compounds* **812**, 152103 (2020).
30. Pang, B. *et al.* Ag nanoparticles incorporated interlayer enables ultrahigh critical current density for Li6PS5Cl-based all-solid-state lithium batteries. *Journal of Power Sources* **563**, 232836 (2023).
31. Wu, M. *et al.* In situ formed LiF-Li3N interface layer enables ultra-stable sulfide electrolyte-based all-solid-state lithium batteries. *Journal of Energy Chemistry* **79**, 272–278 (2023).
32. Subramanian, Y., Rajagopal, R., Kang, S. & Ryu, K.-S. Enhancement of lithium argyrodite interface stability through MoO2 substitution and its application in lithium solid state batteries. *Journal of Alloys and Compounds* **925**, 166596 (2022).

33. Zou, C. *et al.* LiAlO2-coated LiNi0.8Co0.1Mn0.1O2 and chlorine-rich argyrodite enabling high-performance all-solid-state lithium batteries at suitable stack pressure. *Ceramics International* **49**, 443–449 (2023).

34. Subramanian, Y., Rajagopal, R. & Ryu, K.-S. Blending a Li3N/Li3YCl6 solid electrolyte with Li6PS5Cl argyrodite structure to improve interface stability and electrochemical performance in Lithium solid-state batteries. *Journal of Alloys and Compounds* **940**, 168867 (2023).

35. Liu, Y. *et al.* Revealing the Impact of Cl Substitution on the Crystallization Behavior and Interfacial Stability of Superionic Lithium Argyrodites. *Advanced Functional Materials* **32**, 2207978 (2022).

36. Lewis, J. A. *et al.* Role of Areal Capacity in Determining Short Circuiting of Sulfide-Based Solid-State Batteries. *ACS Appl. Mater. Interfaces* **14**, 4051–4060 (2022).

37. Wang, G. *et al.* Hydrolysis-resistant and Anti-dendritic halide composite Li3PS4-LiI solid electrolyte for all-solid-state lithium batteries. *Electrochimica Acta* **428**, 140906 (2022).

38. Zhao, B. *et al.* Stabilizing Li7P3S11/lithium metal anode interface by in-situ bifunctional composite layer. *Chemical Engineering Journal* **429**, 132411 (2022).

39. Wu, M., Liu, G. & Yao, X. Oxygen doped argyrodite electrolyte for all-solid-state lithium batteries. *Applied Physics Letters* **121**, 203904 (2022).

40. Kim, H.-M., Subramanian, Y. & Ryu, K.-S. Improved electrochemical and air stability performance of SeS2 doped argyrodite lithium superionic conductors for all-solid-state lithium batteries. *Electrochimica Acta* **442**, 141869 (2023).

41. Ni, Y., Huang, C., Liu, H., Liang, Y. & Fan, L.-Z. A High Air-Stability and Li-Metal-Compatible Li3+2xP1−xBixS4−1.5xO1.5x Sulfide Electrolyte for All-Solid-State Li–Metal Batteries. *Advanced Functional Materials* **32**, 2205998 (2022).

42. Orsini, F. *et al.* In situ Scanning Electron Microscopy (SEM) observation of interfaces within plastic lithium batteries. *Journal of Power Sources* **76**, 19–29 (1998).

43. Orsini, F. *et al.* In situ SEM study of the interfaces in plastic lithium cells. *Journal of Power Sources* **81–82**, 918–921 (1999).

44. Seong, I. W., Hong, C. H., Kim, B. K. & Yoon, W. Y. The effects of current density and amount of discharge on dendrite formation in the lithium powder anode electrode. *Journal of Power Sources* **178**, 769–773 (2008).

45. Zhou, C. *et al.* Polymorphism, ionic conductivity and electrochemical properties of lithium closo - deca- and dodeca-borates and their composites, Li 2 B 10 H 10 –Li 2 B 12 H 12. *Journal of Materials Chemistry A* **10**, 16137–16151 (2022).

46. Barai, P. *et al.* The Role of Local Inhomogeneities on Dendrite Growth in LLZO-Based Solid Electrolytes. *J. Electrochem. Soc.* **167**, 100537 (2020).

47. Lu, Z. & Ciucci, F. Metal Borohydrides as Electrolytes for Solid-State Li, Na, Mg, and Ca Batteries: A First-Principles Study. *Chem. Mater.* **29**, 9308–9319 (2017).

48. Samsonov, G. V. *Handbook of the Physicochemical Properties of the Elements*. (Springer Science & Business Media, 2012).

49. Tan, D. H. S. *et al.* Carbon-free high-loading silicon anodes enabled by sulfide solid electrolytes. *Science* **373**, 1494–1499 (2021).

50. Randau, S. *et al.* Benchmarking the performance of all-solid-state lithium batteries. *Nat Energy* **5**, 259–270 (2020).

51. Zhou, L. *et al.* High areal capacity, long cycle life 4 V ceramic all-solid-state Li-ion batteries enabled by chloride solid electrolytes. *Nat Energy* **7**, 83–93 (2022).

52. Zhou, L. *et al.* A new halospinel superionic conductor for high-voltage all solid state lithium batteries. *Energy Environ. Sci.* **13**, 2056–2063 (2020).

53. Zhou, L., Assoud, A., Zhang, Q., Wu, X. & Nazar, L. F. New Family of Argyrodite Thioantimonate Lithium Superionic Conductors. *J. Am. Chem. Soc.* **141**, 19002–19013 (2019).

54. Ham, S.-Y. *et al.* Assessing the critical current density of all-solid-state Li metal symmetric and full cells. *Energy Storage Materials* **55**, 455–462 (2023).

55. Stack Pressure Considerations for Room-Temperature All-Solid-State Lithium Metal Batteries - Doux - 2020 - Advanced Energy Materials - Wiley Online Library. https://onlinelibrary.wiley.com/doi/abs/10.1002/aenm.201903253?casa_token=hUbM-mQF3YUAAAAA:3dR0SiRByWsFtUcJaDs3yTH8w7nLt3nEOULPXYDhel91bw0FPxa26yhBf0S4HUpBoXughPneGzHhoil2.

56. LePage, W. S. *et al.* Lithium Mechanics: Roles of Strain Rate and Temperature and Implications for Lithium Metal Batteries. *J. Electrochem. Soc.* **166**, A89 (2019).

57. Ridley, P. *et al.* Glass-Ceramic Sodium-Deficient Chlorides with High Sodium-ion Conductivity. Preprint at https://doi.org/10.26434/chemrxiv-2022-x7llq (2022).